



HAL
open science

Scaling laws of impact induced shock pressure and particle velocity in planetary mantle

J. Monteux, J. Arkani-Hamed

► **To cite this version:**

J. Monteux, J. Arkani-Hamed. Scaling laws of impact induced shock pressure and particle velocity in planetary mantle. *Icarus*, 2016, 264, pp.246-256. 10.1016/j.icarus.2015.09.040 . hal-01637422

HAL Id: hal-01637422

<https://uca.hal.science/hal-01637422>

Submitted on 18 Jan 2018

HAL is a multi-disciplinary open access archive for the deposit and dissemination of scientific research documents, whether they are published or not. The documents may come from teaching and research institutions in France or abroad, or from public or private research centers.

L'archive ouverte pluridisciplinaire **HAL**, est destinée au dépôt et à la diffusion de documents scientifiques de niveau recherche, publiés ou non, émanant des établissements d'enseignement et de recherche français ou étrangers, des laboratoires publics ou privés.

1 **Scaling Laws of Impact Induced Shock Pressure and Particle Velocity in Planetary Mantle**

2
3 **J. Monteux**

4 Laboratoire Magmas et Volcans, Clermont-Ferrand, France

5
6 **J. Arkani-Hamed**

7 Department of Physics, University of Toronto, Toronto, Canada

8 Department of Earth and Planetary Sciences, McGill University, Montreal, Canada

9
10
11
12 **Abstract.** While major impacting bodies during accretion of a Mars type planet have very low
13 velocities (<10 km/s), the characteristics of the shockwave propagation and, hence, the derived
14 scaling laws are poorly known for these low velocity impacts. Here, we use iSALE-2D
15 hydrocode simulations to calculate shock pressure and particle velocity in a Mars type body for
16 impact velocities ranging from 4 to 10 km/s. Large impactors of 100 to 400 km in diameter,
17 comparable to those impacted on Mars and created giant impact basins, are examined. To better
18 represent the power law distribution of shock pressure and particle velocity as functions of
19 distance from the impact site at the surface, we propose three distinct regions in the mantle: a
20 near field regime, which extends to 1-3 times the projectile radius into the target, where the peak
21 shock pressure and particle velocity decay very slowly with increasing distance, a mid field
22 region, which extends to ~ 4.5 times the impactor radius, where the pressure and particle velocity
23 decay exponentially but moderately, and a more distant far field region where the pressure and
24 particle velocity decay strongly with distance. These scaling laws are useful to determine impact
25 heating of a growing proto-planet by numerous accreting bodies.

32 **Introduction:**

33

34 Small planets are formed by accreting a huge number of planetesimals, a few km to a few tens of
35 km in size, in the solar nebula [e.g., Wetherill and Stewart, 1989; Matsui, 1993; Chambers and
36 Wetherill, 1998; Kokubo and Ida, 1995, 1996, 1998, 2000; Wetherill and Inaba, 2000; Rafikov,
37 2003; Chambers, 2004; Raymond, et al., 2006]. An accreting body may generate shock wave if
38 the impact-induced pressure in the target exceeds the elastic Hugoniot pressure, ~ 3 GPa,
39 implying that collision of a planetesimal with a growing planetary embryo can generate shock
40 waves when the embryo's radius exceeds 150 km, assuming that impact occurs at the escape
41 velocity of the embryo and taking the mean density of the embryo and projectile to be 3000
42 kg/m^3 . Hundreds of thousands of collisions must have occurred during the formation of small
43 planets such as Mercury and Mars when they were orbiting the Sun inside a dense population of
44 planetesimal. Such was also the case during the formation of embryos that later were accreted to
45 produce Venus and Earth. Terrestrial planets have also experienced large high velocity impacts
46 after their formation. Over 20 giant impact basins on Mars with diameters larger than 1000 km
47 [Frey, 2008]), the Caloris basin on Mercury with a 1550 km diameter, and the South Pole Aitken
48 basin on Moon with a 2400 km diameter are likely created during catastrophic bombardment
49 period at around 4 Ga. The overlapping Rheasilvia and Veneneia basins on 4-Vesta are probably
50 created by projectiles with an impact velocity of about 5 km/s within the last 1-2 Gy [Keil et al.,
51 1997; Schenk et al., 2012].

52

53

54 The shock wave produced by an impact when the embryo is undifferentiated and completely
55 solid propagates as a spherical wave centered at the impact site until it reaches the surface of the
56 embryo in the opposite side. Each impact increases the temperature of the embryo within a
57 region near the impact site. Because impacts during accretion occur from different directions, the
58 mean temperature in the upper parts of the embryo increases almost globally. On the other hand,
59 the shock wave produced by a large impact during the heavy bombardment period must have
60 increased the temperature in the mantle and the core of the planets directly beneath the impact
61 site, enhancing mantle convection [e.g., Watters et al., 2009; Roberts and Arkani-Hamed, 2012,

62 2014], modifying the CMB heat flux which could in turn favour a hemispheric dynamo on Mars
63 [Monteux et al., 2015], or crippling the core dynamo [e.g., Arkani-Hamed and Olson, 2010a].
64 The impact-induced shock pressure inside a planet has been investigated by numerically solving
65 the shock dynamic equations using hydrocode simulations [e.g., Pierazzo et al., 1997;
66 Wuennemann and Ivanov, 2003; Wuennemann et al., 2006; Bar and Citron, 2011; Kraus et al.,
67 2011; Ivanov et al., 2010; Bierhaus et al., 2012] or finite difference techniques [e.g., Ahrens and
68 O’Keefe, 1987; Mitani, 2003]. However, these numerical solutions demand considerable
69 computer capacity and time and are not practical for investigating the huge number of impacts
70 that occur during the growth of a planet. Hence, the scaling laws derived from field experiments
71 [e.g., Perret and Bass, 1975; Melosh, 1989] or especially from hydrocode simulations [Pierazzo
72 et al., 1997] are of great interest when considering the full accretionary history of a planetary
73 objects [e.g. Senshu et al., 2002, Monteux et al., 2014] or when measuring the influence of a
74 single large impact on the long-term thermal evolution of deep planetary interiors [e.g. Monteux
75 et al., 2007, 2009, 2013, Ricard et al, 2009; Roberts et al., 2009; Arkani-Hamed and Olson,
76 2010a; Arkani-Hamed and Ghods, 2011]. Although the scaling laws provide approximate
77 estimates of the shock pressure distribution, their simplicity and the small differences between
78 their results and those obtained by the hydrocode simulations of the shock dynamic equations
79 (that are likely within the numerical errors that could have been introduced due to the uncertainty
80 of the physical parameters used in the hydrocode models) make them a powerful tool that can be
81 combined with other geophysical approaches such as dynamo models [e.g. Monteux, et al., 2015]
82 or convection models [e.g. Watters et al, 2009; Roberts and Arkani-Hamed, 2012, 2014].

83
84 During the decompression of shocked material much of the internal energy of the shock state is
85 converted into heat leading to a temperature increase below the impact site. The present study
86 focuses on deriving scaling laws of shock pressure and particle velocity distributions in silicate
87 mantle of a planet on the basis of several hydrocode simulations. The scaling laws of Pierazzo et
88 al. [1997] were derived using impact velocities of 10 to 80 km/s, hence may not be viable at low
89 impact velocities. For example, at an impact velocity of 5 km/s, comparable to the escape
90 velocity of Mars, the shock pressure scaling law provides an unrealistic shock pressure that
91 increases with depth. Here we model shock pressure and particle velocity distributions in the
92 mantle using hydrocode simulations for impact velocities of 4 to 10 km/s and projectile

93 diameters ranging from 100 to 400 km, as an attempt to extend Pierazzo et al.'s [1997] scaling
94 laws to low impact velocities and reasonable impactor radii occurring during the formation of
95 terrestrial planets. Hence, on the basis of our scaling laws it is possible to estimate the
96 temperature increase as a function of depth below the impact site for impact velocities
97 compatible with the accretionary conditions of terrestrial protoplanets. These scaling laws can
98 easily be implemented in a multi-impact approach [e.g. Senshu et al, 2003, Monteux et al., 2014]
99 to monitor the temperature evolution inside a growing protoplanet whereas it is not yet possible
100 to adopt hydrocode simulations for that purpose.

101

102 The hydrocode models we have calculated are described in the first section, while the second
103 section presents the scaling laws derived from the hydrocode models. The concluding remarks
104 are relegated to the third section.

105

106 **Hydrocode models of shock pressure distribution:**

107

108 The huge number of impacts during accretion makes it impractical to consider oblique impacts.
109 Not only it requires formidable computer time, but more importantly because of the lack of
110 information about the impact direction, i.e. the impact angle relative to vertical and azimuth
111 relative to north. Therefore, we consider only head-on collisions (vertical impact) to model the
112 thermo-mechanical evolution during an impact between a differentiated Mars size body and a
113 large impactor. We use the iSALE-2D axisymmetric hydrocode, which is a multi-rheology,
114 multi-material hydrocode, specifically developed to model impact crater formation on a
115 planetary scale [Collins et al., 2004, Davison et al., 2010]. To limit computation time, we use a 2
116 km spatial resolution (i.e. more than 25 cells per projectile radius, *cpr*) and a maximum time
117 step of 0.05 s which is sufficient to describe the shockwave propagation through the entire
118 mantle. The minimum post impact monitoring time is set to the time needed by the shockwave to
119 reach the core-mantle boundary (≈ 5 minutes for the impact velocities studied here).

120

121 We investigate the shock pressure and particle velocity distributions inside a Mars size model
122 planet for impact velocities V_{imp} of 4 to 10 km/s and impactors of 100 to 400 km in diameter.
123 Such impactors are capable of creating basins of 1000 to 2500 km in diameter according to

124 Schmidt and Housen [1987] and Holsapple [1993] scaling relationships between the impactor
125 diameter and the resulting basin diameter. These basins are comparable with the giant impact
126 basins of Mars created during the heavy bombardment period at around 4 Ga [Frey, 2008].

127 In our models, the impactor was simplified to a spherical body of radius R_{imp} with uniform
128 composition while the target was simplified to a two layers spherical body of radius R and an
129 iron core radius of R_{core} . The silicate mantle has a thickness of δ_m (See Table 1). We adopt
130 physical properties of silicates (dunite or peridotite) for both the mantle and the impactor to
131 monitor the shock pressure and the particle velocity in a Mars type body. We approximate the
132 thermodynamic response of both the iron and silicate material using the ANEOS equation of
133 state [Thompson and Lauson, 1972, Benz et al., 1989]. To make our models as simple as
134 possible we do not consider here the effects of porosity, thermal softening or low density
135 weakening. However, as a first step towards more realistic models, we investigate the influence
136 of acoustic fluidization and damage. All these effects can be accounted for in iSALE-2D and we
137 will consider each effect in a separate study in near future.

138

139 The early temperature profile of a Mars size body is difficult to constrain because it depends on
140 its accretionary history, on the amount of radiogenic heating and on the mechanisms that led to
141 its core formation [e.g., Senshu et al., 2002]. The uncertainties on the relative importance of
142 these processes as well as the diversity of the processes involved in the core formation lead to a
143 wide range of plausible early thermal states after the full differentiation of Mars. Since we do not
144 consider here the thermal softening during the impact, we assumed the same radially dependent
145 preimpact Martian temperature field in all our simulations. Fig. 1 shows the pre-impact
146 temperature profile as a function of depth. As the pre-impact pressure is governed by the material
147 repartition and as we consider a differentiated Mars, the pre-impact pressure is more
148 straightforward. Fig. 1 also shows the pre-impact hydrostatic pressure used in our models as a
149 function of depth considering a 1700 km thick silicate mantle surrounding a 1700 km radius iron
150 core. We emphasize that the peak pressure shown in our study does not include this hydrostatic
151 pressure. However, the hydrostatic pressure is taken into consideration in calculating the
152 hydrocode models. The peak pressure presents the shock induced pressure increase and is
153 expected to depend on the physical properties of the target, but not on the size of the target as
154 long as the size is large enough to allow shock wave propagates freely without interference with

155 reflected waves. A scaling law should reflect the properties of the shock wave propagation in a
156 uniform media. Fig. 2 shows the typical time evolution of the compositional and pressure fields
157 after a 100 km diameter impact with $V_{\text{imp}}=10$ km/s. Immediately after the impact, the shockwave
158 propagates downward from the impact site. The shock front reaches the core-mantle boundary in
159 less than 5 minutes while the transient crater is still opening at the surface. It is worth mentioning
160 that the main goal is to derive a scaling law which is useful for numerous impacts during
161 accretion where no information is available about the impact direction, i.e. the impact angle
162 relative to vertical and azimuth relative to north. Moreover, the pressure reduction near the
163 surface due to interference of the direct and reflected waves can easily be accommodated
164 following the procedure by Melosh [1989], which is adapted to spherical surface by Arkani-
165 Hamed [2005], when applying the scaling law to a particular accretion scenario.

166
167 In Fig. 3, we monitor the peak pressure as a function of the distance from the impact site d
168 normalized by the impactor radius R_{imp} along the symmetry axis for the case illustrated in Fig. 2.
169 In our iSALE models, the impact-induced pressure fields (as well as temperature and velocity
170 fields) are extracted from a cell-centered Eulerian grid data. To validate our models, we have
171 tested different spatial resolutions expressed here in terms of cells per projectile radius (c_{ppr}). In
172 Fig. 3a, we represent the peak pressure decrease as a function of depth for c_{ppr} values ranging
173 from 5 to 50, showing convergence for c_{ppr} values larger than 25. As illustrated in Fig. 3a, the
174 difference between the results with 25 and 50 c_{ppr} is less than 10%. This resolution study is in
175 agreement with Pierazzo et al., [2008] who have shown that the iSALE models converge for
176 resolutions of 20 c_{ppr} or higher, although a resolution of 10 c_{ppr} still provides reasonable results
177 (a resolution of 20 c_{ppr} appears to underestimate peak shock pressures by at most 10%). The
178 resolution is 25 c_{ppr} or higher in our models.

179 In Pierazzo et al., [1997], the impactor radius ranged between 0.2 and 10 km. In Fig. 3b, we
180 compare our results obtained with $R_{\text{imp}}=10$ km, $R_{\text{imp}}=50$ km and the results obtained by Pierazzo
181 et al., [1997]. Fig. 3b shows that even with a radius of 50 km, both our results and the results
182 from Pierazzo et al., [1997] are in good agreement, confirming that the impactor size has minor
183 effects on the peak pressure evolution with depth. The small differences between our results with
184 different impactor radii (discussed further in more details) are plausibly the direct consequence
185 of using increasing c_{ppr} values with increasing impactor radii. Consequently, we will use the

186 normalized distance in all of our figures, as equations of motion should be invariant under
187 rescaling of distance [Melosh, 1989, Pierazzo et al, 1997]. However, to monitor the peak
188 pressure evolution with $R_{\text{imp}}=10$ km and to maintain a reasonable computational time, we have
189 used only 10 *cppr*. This figure confirms that below 10 *cppr*, the spatial accuracy is insufficient
190 and our results diverge from the results obtained by Pierazzo et al., [1997].

191 **Shock pressure and particle velocity scaling laws at low impact velocities:**

192
193 A given hydrocode simulation may take on the order of 48 hours to determine a 2D shock
194 pressure and particle velocity distributions in the mantle of our model planet. The impact
195 velocity is about 4 km/s for a protoplanet with a radius of 2860 km and mean density of 3500
196 kg/m^3 , assuming that impacts occur at the escape velocity of the protoplanet. Mars is more likely
197 a runaway planetary embryo formed by accreting small planetesimals and medium size
198 neighboring planetary embryos. This indicates that the accreting bodies had velocities higher
199 than 4 km/s when Mars was growing from 2860 km radius to its present radius of about 3400
200 km. Taking the mean radius of the impacting bodies to be 100 km, which is larger than that of a
201 typical planetesimal, more than 15,000 bodies must have accreted at impact velocities higher
202 than 4 km/s. Calculating the impact induced shock pressure and particle velocity inside the
203 growing Mars would be formidable if hydrocode simulation is adopted for each impact.
204 Because the impact-induced shock pressure P and particle velocity V_p inside a planetary mantle
205 decrease monotonically with distance from the impact side, simple exponential functions have
206 been proposed to estimate peak pressure and particle velocity in the mantle of an impacted body.
207 Solving the shock dynamic equations by a finite difference technique for silicate target and
208 projectile, Ahrens and O'Keefe [1987] showed that pressure distribution in the target displays
209 three regimes: an impedance match regime, Regime I, which extends to 1-3 times the projectile
210 radius into the target where the peak shock pressure is determined by the planar impedance
211 match pressure [McQueen et al., 1970]; a shock pressure decay regime, Regime II, where the
212 pressure decays exponentially as

$$213$$
$$214 P = P_o (d/R_{\text{imp}})^n, \quad \text{for } d > 1-3 \text{ times } R_{\text{imp}}, \text{ and } n = -1.25 - 0.625 \text{ Log}(V_{\text{imp}}), \quad (1)$$
$$215$$

216 and the elastic regime, Regime III, where the shock pressure is reduced below the strength of
 217 target, the Hugoniot elastic limit, and the shock wave is reduced to an elastic wave with pressure
 218 decaying as d^{-3} . In equation (1) d is the distance from the impact site at the surface, R_{imp} is the
 219 projectile radius, and V_{imp} is the impact velocity in km/s. The peak pressure measurements in the
 220 nuclear explosions [Perret and Bass, 1975] led Melosh [1989] to propose a scaling law for the
 221 particle velocity distribution assuming conservation of momentum of the material behind the
 222 shock front which is taken to be a shell of constant thickness. Using several different target
 223 materials, and adopting hydrocode simulations Pierazzo et al. [1997] showed that the shock
 224 pressure P and particle velocity V_p decrease slowly in the near field zone, but rapidly in the
 225 deeper region,

$$226$$

$$227 \quad P = P_{\text{ic}} (d_{\text{ic}}/d)^n, \quad n = -1.84 + 2.61 \text{Log}(V_{\text{imp}}), \quad d > d_{\text{ic}} \quad (2a)$$

$$228 \quad V_p = V_{\text{pic}} (d_{\text{ic}}/d)^m \quad m = -0.31 + 1.15 \text{Log}(V_{\text{imp}}), \quad d > d_{\text{ic}} \quad (2b)$$

229

230 The authors coined an isobaric zone of shock pressure P_{ic} and particle velocity V_{pic} for the near
 231 field of radius d_{ic} , about $1.5 R_{\text{imp}}$. Equations 2a and 2b were derived by averaging results from
 232 many different materials and impactor sizes. The impact velocities adopted were 10 to 80 km/s
 233 and the projectile diameter ranged from 0.4 to 20 km.

234

235 In a log-log plot the peak shock pressure and the corresponding particle velocity are linear
 236 functions of distance from the impact site,

$$237$$

$$238 \quad \text{Log } P = a + n \text{Log}(d/R_{\text{imp}}) \quad (3a)$$

$$239 \quad \text{Log } V_p = c + m \text{Log}(d/R_{\text{imp}}) \quad (3a)$$

240

241 where a is the logarithm of pressure and c is the logarithm of particle velocity both at R_{imp} and n
 242 and m are decay factors. All parameters are impact velocity dependent:

$$243$$

$$244 \quad a = \alpha + \beta \text{Log}(V_{\text{imp}}) \quad (4a)$$

$$245 \quad c = \gamma + \Omega \text{Log}(V_{\text{imp}}) \quad (4b)$$

246

247 and

$$248 \quad n = \lambda + \delta \text{Log} (V_{\text{imp}}) \quad (5a)$$

$$249 \quad m = \eta + \zeta \text{Log} (V_{\text{imp}}) \quad (5b)$$

250

251 Figure 4 shows the peak shock pressure inside the mantle of the model planet we obtained by
252 hydrocode simulation and using a projectile of 100 km diameter at 10 km/s impact velocity.
253 There is actually no isobaric region, rather the peak pressure decays slowly in the near field zone
254 but much rapidly in the deeper parts, similar to the results by Ahrens and O’Keefe [1987].
255 Although the regression lines fitted to the near field and far field are good representatives of the
256 shock pressure distribution, they intersect at a much higher pressure than that of the hydrocode
257 model and overestimate the pressure by as much as 30% in a large region located between the
258 near field and the far field. Therefore, to better approximate the pressure distribution we fit the
259 pressure curve by three lines, representing the near field, mid field and far field regions, which
260 render a much better fit as seen in Figure 4.

261

262 Figure 5a shows the peak shock pressure versus distance from the impact site for impact
263 velocities of 4 to 10 km/s and an impactor of 100 km in diameter. Because of different
264 phenomenon such as excavation, melting, vaporization and intermixing between the target and
265 projectile material, the shock front in near field is more difficult to characterize by our numerical
266 models even for high *cppr*. Also, as the shock wave is not yet detached from the impactor, it
267 cannot be treated as a single shock wave. Hence, the near field - mid field boundary and the
268 scaling laws for the near field are less accurate than for the two other fields especially for large
269 impact velocities ($V_{\text{imp}} > 7$ km/s). In Figure 5, the larger dots show the intersections of the linear
270 regression lines. For example a dot that separates near field from mid field is the intersection of
271 the regression lines fitted to the near field and midfield. The regression lines are determined
272 from fitting to the hydrocode data. Visually, we first divide the hydrocode data of a given model
273 into three separate sections with almost linear trends, and then fit the regression lines to those
274 three trends. Figure 5a shows the hydrocode data, small dots, and the regression lines,
275 demonstrating the tight fitting of the lines to the data. The large dots in the figure show the
276 intersection of the regression lines of the adjacent regions. For example the dot that shows the
277 near-field mid-field boundary is the intersection of the regression lines fitted to the near field and

278 mid field hydrocode data. Note that a big dot does not necessarily coincide with the exact
279 hydrocode result, a small dot. As the near field – mid field boundary is relatively less resolved,
280 Figure 5a shows a scatter of the dots separating those two fields and a slight slope change from
281 $V_{\text{imp}} > 7$ km/s. In the average the near field – mid field boundary is at $\sim 2.3 R_{\text{imp}}$ (~ 115 km) from
282 the impact site. Figure 5a shows that the depth to the mid field – far field boundary is almost
283 independent of the pressure. It is at about $4.5 R_{\text{imp}}$ (~ 225 km) from the impact site.

284

285 We propose three scaling laws for shock pressure, and three for particle velocity:

$$286 \quad \text{Log } P_i = a_i + n_i \text{Log}(d_i / R_{\text{imp}}), \quad i=1, 2, \text{ and } 3. \quad (6a)$$

$$287 \quad \text{Log } V_{pi} = c_i + m_i \text{Log}(d_i / R_{\text{imp}}), \quad i=1, 2, \text{ and } 3. \quad (6b)$$

288

289 For the near field $d_i < 2.3 R_{\text{imp}}$, mid field $2.3 R_{\text{imp}} < d_i < 4.5 R_{\text{imp}}$, and far field $d_i > 4.5 R_{\text{imp}}$. Table
290 2 lists the values of the parameters in the above equations as well as the misfits obtained from
291 our regressions (smaller than 0.001 in all the regressions calculated here). Figure 5a shows the
292 three regression lines fitted to the near field, mid field, and far field of each model for shock
293 pressure, and Figure 5b displays those for particle velocity. The misfits from Table 2 are based
294 on the fixed end points, shown as dots in Fig. 5.

295

296 The close agreement between Pierazzo et al. [1997] model for impact velocity of 10 km/s
297 derived by averaging results of impactors with diameters 0.4 to 20 km, and our result for the
298 same impact velocity but an impactor of 100 km in diameter indicates that the shock pressure
299 distribution is less sensitive to impactor size in a log-log plot of pressure versus distance
300 normalized to the impactor radius. To further investigate this point, we calculate models with
301 impactor sizes of 100 to 400 km in diameter. Figure 6a shows the hydrocode results for impact
302 velocity of 10 km/s using different impactor size. The result obtained for $R_{\text{imp}}=10$ km is not
303 included in the figure because of its low *cppr* value (see Fig. 3b). The curves have almost the
304 same slope in the far field, and small deviations in the mid field and near field.

305

306 Pierazzo et al. [1997] used several different rock types for the solid mantle and concluded that
307 their scaling laws are less sensitive to the rock types. Bearing in mind that dunite and peridotite
308 are probably the most representative rocks for solid mantle, we run a hydrocode model using an

309 impactor of 100 km in diameter, impact velocity of 10 km/s, and peridotite as a representative
310 mantle and impactor rock. Figure 6b compares the results for the dunite and peridotite models.
311 They are indeed very similar, especially in the far field region, where the exponential factor n in
312 Equation (3a) is -1.449 for dunite and -1.440 for peridotite. The major differences between the
313 two models arise from the near field zone, hence propagates down to the deeper regions.

314

315 Among the other parameters and phenomenon that may influence the shockwave propagation
316 (porosity, thermal softening...), accounting for the acoustic fluidization is required to accurately
317 simulate the formation of a complex crater [e.g., Melosh, 1979, Bray et al., 2008, Potter et al.,
318 2012]. Indeed, acoustic fluidization is invoked to explain the collapse of complex craters by
319 modifying the frictional strength of the damaged target. Figure 6c compares the results obtained
320 for $R_{\text{imp}}=50$ km and $V_{\text{imp}}=10$ km/s considering acoustic fluidization and an Ivanov damage model
321 which prescribes damage as a function of plastic strain. This figure shows that for the near and
322 mid fields, the results are similar. Pierazzo et al. [1997] did not include acoustic fluidization or
323 damage in their models. Hence, our results without acoustic fluidization or damage model and
324 the results from Pierazzo are in good agreement (Fig. 6c). As soon as the far field is reached,
325 acoustic fluidization and damage tend to reduce the intensity of the shock pressure. This
326 indicates that building more sophisticated models will be necessary in the near future. As the
327 impact heating is mainly localized in the near- and mid-fields, including a damage model or
328 acoustic fluidization should only weakly affect the thermal evolution of a growing protoplanet.
329 However, it is worth mentioning that we are not concerned with the shape of the crater produced
330 by a large impact, rather the main goal of our study is to extend the scaling laws of Pierazzo et
331 al., [1997] to lower impact velocities which are more compatible with accretionary conditions.

332

333 Figure 7 shows the impact velocity dependence of a , n , c , and m . Also included in Figure 7b is
334 the model by Ahrens and O'Keefe [1987] which was derived using impact velocities of 5 km/s
335 and higher. Pierazzo et al. [1997] used impact velocities higher than those considered in the
336 present study, except for their 10 km/s model. Hence, their results are shown in Figure 7b by
337 only one point, asterisk, at the impact velocity of 10 km/s.

338

339 The shock pressure along a non-vertical profile is not supposed to be the same as the one along a

340 vertical profile, largely because of the pre-impact lithostatic pressure. As emphasized by
341 Pierazzo et al. [1997, 2008] the shock front in deeper regions appears relatively symmetric
342 around the impact point. Of course, it is not realistic in the case of an oblique impact (not
343 studied here) and for the shallowest angles where the surface significantly affects the shock
344 pressure decay. We have monitored the effect of the shockwave propagation angle θ with values
345 varying between 90° (vertical profile) to 27° (Fig. 8). Similarly to Pierazzo et al [1997], we did
346 not find a significant angle dependence on our results especially when θ is ranging between 90°
347 and 45° . For smaller values of θ , the surface effects appear to modify the shockwave propagation
348 by reducing its intensity (Fig. 8 a). Except in the mid field, where the n value decreases from -0.6
349 to -1.31, and in the far field, where the a value decreases from 2.54 to 1.93, the coefficients a and
350 n from our scaling laws do not change significantly with the angle (Fig. 8 b). This is particularly
351 true in the near field where most of the impact heating occurs.

352
353 Scaling laws have been used by many investigators [e.g., Senshu et al., 2002; Tonks and Melosh,
354 1992, 1993; Watters et al, 2009; Roberts et al., 2009; Arkani-Hamed and Olson, 2010a, 2010b;
355 Arkani-Hamed and Ghods, 2011], mainly because they require a much smaller computer and
356 much less computer time and the difference between a hydrocode model and a corresponding
357 scaling model is minute. For example, Figure 9 shows the 2D distribution of the peak shock
358 pressure determined for an impactor of 100 km in diameter and an impact velocity of 10 km/s
359 calculated using our scaling laws in near field, mid field, and far field, and the parameter values
360 from Table 2. The grid spacing is 2 km in radial direction and 0.03 degrees in the colatitude
361 direction. The entire computer time in a PC, CPU: 2.4 GHz, was only 16 seconds, which also
362 calculated the 2D distribution of shock-induced temperature increase using Watters et al.'s
363 [2009] foundering shock heating model. The computer time is substantially shorter than 48
364 hours taken by our corresponding hydrocode model using a CPU: 2.9 GHz laptop. This shows
365 that it is feasible to determine impact heating during the accretion of a terrestrial planet using
366 scaling laws, whereas it is almost impossible to adopt hydrocode simulations for that purpose.

367
368 During the decompression of shocked material much of the internal energy of the shock state is
369 converted into heat [O'Keefe and Ahrens, 1977]. Using thermodynamic relations, the waste heat
370 used to heat up the impacted material can be estimated [Gault and Heitowit, 1963; Watters et al.,

2009] and the corresponding temperature increase ΔT can be obtained. Hence, on the basis of our scaling laws it is possible to estimate the temperature increase as a function of depth below the impact site for impact velocities compatible with the accretionary conditions of terrestrial protoplanets. These scaling laws can easily be implemented in a multi-impact approach [e.g. Senshu et al, 2003, Monteux et al., 2014] to monitor the temperature evolution inside a growing protoplanet whereas it is not yet possible to adopt hydrocode simulations for that purpose. For example, included in Figure 9 is the impact induced temperature increase corresponding to the shock pressure shown in the figure. The temperature increase is determined on the basis of foundering model of Watters et al. [2009] using constant values for the acoustic velocity C (6600 m/s) and the parameter S (0.86) in their expressions:

$$\Delta T(P) = \frac{P}{2\rho_0 S} (1 - f^{-1}) - (C/S)^2 [f - \ln f - 1] \quad (7)$$

$$f(P) = -\frac{P}{\beta} \left(1 - \sqrt{\frac{2P}{\beta} + 1} \right)^{-1} \quad (8)$$

$$\beta = \frac{C^2 \rho_0}{2S} \quad (9)$$

with P the shock-increased pressure and ρ_0 the density prior to shock compression (see Tab. 1 for values).

Due to small size the impactor is not capable of increasing the lower mantle temperature of the model planet significantly, and only minor impact heating of the core has occurred. The thermal evolution model has to be combined to a topographical evolution model to account for the growth of the protoplanet as in Monteux et al., [2014]. In these models, the impact angle (considered here as vertical) probably plays a key role because it influences both the morphology of the impact heating and the shape of the post-impact topography. A more elaborated scaling laws built upon 3D hydrocode models will be developed for that purpose in the near future.

It is worth emphasizing that our scaling laws, like those of others [Ahrens and O'Keefe, 1987; Pierazzo et al., 1997; Mitani, 2003], are derived from a few hydrocode models. Figure 10 shows the profiles of the pressure along the axis of symmetry for comparison. The differences between

400 the hydrocode model and the scaling law are small for the most part, but the exact scaling law
401 differs by ~ 10 GPa for $d/R_{\text{imp}} = 2-3$. This difference arises from the difficulty of correctly
402 describe the near field as previously mentioned. Note that the interpolated model is in much
403 better agreement with the hydrocode model.

404
405 A linear relationship has been proposed between the shock wave velocity V_s and particle velocity
406 V_p on the basis of laboratory measurements [McQueen, 1967; Trunin, 2001]

$$408 \quad V_s = C + S V_p \quad (10)$$

409
410 where C is the acoustic velocity and S is a constant parameter. We estimate the acoustic velocity
411 in the mantle of the model planet on the basis of our hydrocode models (Figure 5a, 5b) using
412 Equation (10) and the Hugoniot equation

$$414 \quad P = \rho V_p V_s \quad (11)$$

415
416 where $\rho (=3320 \text{ kg/m}^3)$ is the pre-shock density. Figure 11 shows the variations of C with depth
417 for models with impact velocities of 4 to 10 km/s and an impactor of 100 km diameter, using
418 $S=1.2$ which is within the values proposed by the authors for dunite [e.g., Trunin, 2001].
419 Adopting $S=0.86$ [McQueen, 1967] does not change the results significantly, especially in the far
420 field, where the acoustic velocity is less sensitive to particle velocity and linearly increases with
421 depth. However C shows particle velocity dependence in the mid field and near field.

423 **Conclusions:**

424
425 We have modeled the shock pressure and particle velocity distributions in the mantle of a Mars
426 size planet using hydrocode simulations (iSALE-2D) for impact velocities of 4 to 10 km/s and
427 projectile diameters ranging from 100 to 400 km. We have extended Pierazzo et al.'s [1997]
428 scaling laws to low impact velocities and also considered large impactor radii occurring during
429 the formation of terrestrial planets. We propose three distinct regions in the mantle: a near field
430 region, which extends to 1-3 times the projectile radius into the target, where the peak shock

431 pressure and particle velocity decay very slowly with increasing distance, a mid field region,
432 which extends to ~ 4.5 times the impactor radius, where the pressure and particle velocity decay
433 exponentially but moderately, and a more distant far field region where the pressure and particle
434 velocity decay strongly with distance. The mid field – far field boundary is well constrained,
435 whereas that of the near field - mid field is a relatively broad transition zone for the impact
436 velocities examined.

437

438 **Acknowledgements:** This research was supported by Agence Nationale de la Recherche
439 (Oxydeep decision No. ANR-13-BS06-0008) to JM, and by Natural Sciences and Engineering
440 Research Council (NSERC) of Canada to JAH. We gratefully acknowledge the developers of
441 iSALE (www.isale-code.de), particularly the help we have received from Gareth S. Collins. We
442 are also grateful to the two reviewers for very helpful suggestions.

443

444 **References:**

445 Ahrens, T.J., J.D., O’Keefe, (1987). Impact on the Earth, ocean and atmosphere. *Int. J. Impact*
446 *Eng.* 5, 13–32. 122.

447 Arkani-Hamed, J., Magnetic crust of Mars, *J. Geophys. Res.*, 110, E08005,
448 doi:10.1029/2004JE002397, 2005.

449 Arkani-Hamed, J, and A. Ghods, (2011). Could giant impacts cripple core dynamos of small
450 terrestrial planets?, *Icarus* 212, 920–934.

451 Arkani-Hamed, J., Olson, P., (2010a). Giant Impact Stratification of the Martian Core *Geophys.*
452 *Res. Let.*, 37, L02201, doi:10.1029/2009GL04141

453 Arkani-Hamed, J., Olson, P., (2010b). Giant impacts, core stratification, and failure of the
454 Martian dynamo. *J. Geophys. Res.* 115, E07012.

455 Barr, A., Citron, R., (2011). Scaling of melt production in hypervelocity impacts from high-
456 resolution numerical simulations, *Icarus* 211, 913–916.

457 Benz, W., Cameron, A.G.W., Melosh, H.J., (1989). The origin of the Moon and the single-
458 impact hypothesis III. *Icarus* 81, 113–131.

459 Bierhaus, M., K. Wünnemann, and D. Elbeshausen, (2012). Numerical modeling of basin-
460 forming impacts: implications for the heat budget of planetary interiors, 43rd Lunar and
461 Planetary Science Conference. Abstract # 2174.pdf.

462 Bray, V. J., Collins, G. S., Morgan, J. V., Schenk, P. M., (2008). The effect of target properties
463 on crater morphology: comparison of central peak craters on the Moon and Ganymede.
464 *Meteoritics & Planetary Science*. 43, 1979-1992.

465 Chambers, J.E., (2004). Planetary accretion in the inner Solar System, *Earth Planet. Sci. Lett.*
466 223, 241–252.

467 Chambers, J.E., and G. W. Wetherill, (1998). Making the terrestrial planets: N-Body integrations
468 of planetary embryos in three dimensions, *Icarus*, 136, 304–327.

469 Collins, G. S., H. J. Melosh, and B. A. Ivanov (2004), Modeling damage and deformation in
470 impact simulations, *Meteoritics Planet. Sci.*, 39(2), 217–231, doi:10.1111/j.1945-
471 5100.2004.tb00337.x.

472 Davison, T. M., G. S. Collins, and F. J. Ciesla (2010), Numerical modeling of heating in porous
473 planetesimal collisions, *Icarus*, 208, 468–481, doi:10.1016/j.icarus.2010.01.034.

474 Frey, H. (2008), Ages of very large impact basins on Mars: Implications for the late heavy
475 bombardment in the inner solar system, *Geophys. Res. Lett.*, 35, L13203,
476 doi:10.1029/2008GL033515.

477 Gault, D. E., and E. Heitowit (1963), The partition of energy for hypervelocity impact craters
478 formed in rock, paper presented at 6th Hypervelocity Impact Symposium, Firestone Tire
479 and Rubber Co., Cleveland, 30 Apr. to 2 May.

480 Holsapple, K. A. (1993), The scaling of impact processes in planetary sciences, *Annu. Rev.*
481 *Earth Planet. Sci.*, 21, 333–373.

482 Ivanov, B.A., H.J. Melosh, and E. Pierazzo, (2010). Basin-forming impacts: Reconnaissance
483 modeling, *Geological Society of America, Special Paper* 465, 29-49.

484 Keil, K., D. Stoffer, S. G. Love, E. R. D. Scott (1997), Constraints on the role of impact heating
485 and melting in asteroids, *Meteorit. Planet. Sci.*, 32, 349-363.

486 Kokubo, E. and S. Ida, (1995). Orbital evolution of protoplanets embedded in a swarm of
487 planetesimals, *Icarus*, 114, 247-257.

488 Kokubo, E. and S. Ida, (1996). On Runaway Growth of Planetesimals, *Icarus*, 123, 180–191.

489 Kokubo, E. and S. Ida, (1998). Oligarchic Growth of Protoplanets, *Icarus*, 131, 171–178.

490 Kokubo, E. and S. Ida, (2000). Formation of protoplanets from planetesimals in the solar nebula,
491 Icarus 143, 15–27.

492 Kraus, R. G., L. E. Senft, and S. T. Stewart, (2011). Impacts onto H₂O Ice: Scaling Laws for
493 Melting, Vaporization, Excavation, and Final Crater Size, Icarus, 214, 724-738.

494 Matsui, T., (1993). Early evolution of terrestrial planets: Accretion, atmospheric formation, and
495 thermal history, in Primitive Solar Nebula and Origin of Planets, Edt. H. Oya, pp 545-
496 559, Terra Scientific Publication Company, Tokyo.

497 McQueen, R. G., S. P. Marsh, J. W. Taylor, J. N. Fritz, and W. J. Carter (1970). The equation of
498 state of solids from shock wave studies. In Kinslow (Ed.), *High Velocity Impact*
499 *Phenomena*, Academic, New York, pp. 294-491.

500 McQueen, R.G., Marsh, S.P., Fritz, J.N., 1967. Hugoniot equation of state of twelve rocks. J.
501 Geophys. Res. 72, 4999–5036. Melosh, H. J. 1989. Impact Cratering: A Geologic Process,
502 Oxford Univ. Press, New York.

503 Melosh H. J. (1979), Acoustic fluidization: A new geologic process? J. Geophys. Res., 84, 7513–
504 7520.

505 Melosh, M. J. (1989), Impact Cratering: A Geological Process, 1st ed., Oxford Univ. Press, New
506 York.

507 Mitani, N. K. (2003), Numerical simulations of shock attenuation in solids and reevaluation of
508 scaling law, *J. Geophys. Res.*, 108, (E1), 5003, doi:10.1029/2000JE001472.

509 Monteux, J., N. Coltice, F. Dubuffet, Y. Ricard (2007), Thermo-mechanical adjustment after
510 impacts during planetary growth, *Geophys. Res. Lett.*, 34, L24201,
511 doi:10.1029/2007GL031635

512 Monteux, J., Y. Ricard, N. Coltice, F. Dubuffet, M. Ulvrova (2009), A model of Metal-Silicate
513 separation on Growing Planets, *Earth and Planet. Sci. Lett.*, 287, 353-362,
514 doi:10.1016/j.epsl.2009.08.020

515 Monteux, J., M. Jellinek, C. J., Johnson, (2013) Dynamics of core merging after a martian mega-
516 impact, *Icarus*, 226, Issue 1, Pages 20–32, doi:10.1016/j.icarus.2013.05.008

517 Monteux, J., G., Tobie, G., Choblet, M., Le Feuvre (2014), Can large icy Moons accrete
518 undifferentiated?, *Icarus*, 237, 15 July 2014, Pages 377-387,
519 doi:10.1016/j.icarus.2014.04.041

520 Monteux, J., Amit, H., Choblet, G., Langlais, B., Tobie, G. (2015) Giant impacts, heterogeneous
521 mantle heating and a past hemispheric dynamo on Mars, *Phys. Earth Planet. Int.*, 240,
522 114-124 doi:10.1016/j.pepi.2014.12.005.

523 O’Keefe, J. D., and T. J. Ahrens (1977), Impact-induced energy partitioning, melting, and
524 vaporization on terrestrial planets, *Lunar Planet. Sci. Conf.*, 8th, 3357–3374.

525 Perret, W.R., and R.C. Bass, (1975). Free-Field ground motion induced by underground
526 explosions. Sandia Report SAND74-0252.

527 Pierazzo, E., Vickery, A.M., and Melosh, H.J., (1997). A re evaluation of impact melt
528 production. *Icarus* 127, 408–423.

529 Pierazzo, E., Artemieva, N., Asphaug, E., Baldwin, E.C., Cazamias, J., Coker, R., Collins, G.S.,
530 Crawford, D.a., Davison, T., Elbeshausen, D., Holsapple, K.a., Housen, K.R.,
531 Korycansky, D.G., Wünnemann, K., (2008), Validation of numerical codes for impact
532 and explosion cratering: impacts on strengthless and metal targets. *Meteorit. Planet. Sci.*
533 43 (12), 1917–1938.

534 Potter, R., Kring, D.A., Collins, G.S., Kiefer, W., McGovern, P., (2012). Estimating transient
535 crater size using the crustal annular bulge: Insights from numerical modeling of lunar
536 basin-scale impacts. *Geophys. Res. Lett.* 39, L18203

537 Rafikov, R.R., (2003). The growth of planetary embryos: Orderly, runaway, or oligarchic, *The*
538 *Astron. J.*, 125, 942–961.

539 Raymond, S.N., T. Quinn, and J. I. Lunine, (2006). High-resolution simulations of the final
540 assembly of Earth-like planets, *Terrestrial accretion and dynamics*, *Icarus* 183, 265–282.

541 Ricard, Y., Srámek, O., Dubuffet, F., (2009). A multi-phase model of runaway core-mantle
542 segregation in planetary embryos. *Earth Planet Sci. Lett.* 284, 144–150.

543 Roberts, J.H., and J. Arkani-Hamed, (2012). Impact-induced mantle dynamics on Mars, *Icarus*
544 218, 278–289.

545 Roberts, J.H., and J. Arkani-Hamed, (2014). Impact heating and coupled core cooling and
546 mantle dynamics on Mars, *J. Geophys. Res. Planets*, 119, 729-744,
547 doi:10.1002/2013JE004603.

548 Roberts, J.H., R.J. Lillis, and M. Manga (2009). Giant impacts on early Mars and the cessation of
549 the Martian dynamo. *J. Geophys. Res.* 114, E04009.

550 Schenk, P. et al. (2012), The Geologically Recent Impact Basins at Vesta's South Pole, *Science*,
551 336, 694-697.

552 Senshu, H., K. Kuramoto, and T. Matsui, (2002). Thermal evolution of a growing Mars, *J.*
553 *Geophys. Res.*, 107, E12, 5118, doi:10.1029/2001JE001819.

554 Schmidt, R. M., and K. R. Housen (1987), Some recent advances in the scaling of impact an
555 explosion cratering, *Int. J. Impact Eng.*, 5, 543– 560.

556 Thompson, S., Lauson, H., 1972. Improvements in the CHART D Radiation-hydrodynamic Code
557 III: Revised Analytic Equations of State. Sandia National Laboratory Report SC-RR-71
558 0714, 113p.

559 Tonks, W.B., and H.J. Melosh, (1992). Core Formation by Giant Impacts, *Icarus* 100, 326-346.

560 Tonks, W.B., and H.J. Melosh, (1993). Magma Ocean Formation Due to Giant Impacts, *J.*
561 *Geophys. Res.*, 98, 5319-5333.

562 Trunin, R.F., 2001. Experimental Data on Shock Compression and Adiabatic Expansion of
563 Condensed Matter. RFNC-VNIIEF, Sarov, p. 446, ISBN 5-85165-624-7.

564 Watters W.A., Zuber, M.T., Hager, B.H. (2009). Thermal perturbations caused by large impacts
565 and consequences for mantle convection, *J. Geophys. Res.*, 114, E02001

566 Wetherill, G.W., Inaba, S., (2000). Planetary accumulation with a continuous supply of
567 planetesimals, *Space Sci. Rev.* 92, 311-320].

568 Wetherill, G.W., and G. R. Stewart, (1989). Accumulation of a Swarm of Small Planetesimals,
569 *Icarus* 77, 330-357.

570 Wünnemann K., and B.A. Ivanov (2003). Numerical modelling of impact crater depth-diameter
571 dependence in an acoustically fluidized target, *Planet. and Space Sci.*, 51, 831-845.

572 Wünnemann K., G.S., Collins, and H. J. Melosh (2006). A strain-based porosity model for use in
573 hydrocode simulations of impacts and implications for transient-crater growth in porous
574 targets, *Icarus* 180, 514-52.

575

576

577

578

579

580

581 **Table List:**

582

583 Table 1. Typical parameter values for numerical hydrocode models

584

Target radius	R	3400 km
Target core radius	R_{core}	1700 km
Silicate mantle thickness	δ_{m}	1700 km
Impactor radius	R_{imp}	50-200 km
Impact velocity	V_{imp}	4-10 km/s
<i>Mantle properties (Silicates)</i>		
Initial density	ρ_{m}	3314 kg/m ³
Equation of state type		ANEOS
Poisson		0.25
Strength Model		Rock
(iSALE parameters)		($Y_{i0}=10$ MPa, $\mu_i=1.2$, $Y_{im}=3.5$ GPa)
Acoustic Fluidization Model		Block
(iSALE parameters)		($t_{\text{off}}=16$ s, $c_{\text{vib}}=0.1$ m/s, $\text{vib}_{\text{max}}=200$ m/s)
Damage Model		Ivanov
(iSALE parameters)		($\epsilon_{\text{fb}}=10^{-4}$, $B=10^{-11}$, $p_c=3 \times 10^8$ Pa)
Thermal softening and porosity models		None
<i>Core properties (Iron)</i>		
Initial density	ρ_{c}	7840 kg/m ³
Equation of state type		ANEOS
Poisson		0.3
Strength Model		Von Mises
(iSALE parameters)		($Y_0=100$ MPa)
Acoustic Fluidization Model		Block
(iSALE parameters)		($t_{\text{off}}=16$ s, $c_{\text{vib}}=0.1$ m/s, $\text{vib}_{\text{max}}=200$ m/s)
Damage, thermal softening and porosity models		None

585
586
587
588
589
590
591
592
593
594
595
596
597
598
599
600
601
602
603
604
605
606
607
608
609
610
611
612
613
614
615
616
617
618
619
620
621
622
623
624
625
626
627
628
629

Table 2. Parameters of the peak shock pressure distribution and the corresponding particle velocity in the mantle of the Mars size model planet. The pressure is expressed as:

$$\text{Log}(P) = a + n \text{Log}(d/R_{\text{imp}})$$

and the particle velocity as:

$$\text{Log}(V_p) = c + m \text{Log}(d/R_{\text{imp}})$$

where the pressure P is in GPa, the particle velocity V_p is in km/s, d is the distance from the impact site at the surface, and R_{imp} is the impactor radius. a and c are the logarithm of pressure and particle velocity at the distance R_{imp} from the impact site, and n and m are the decay exponents of pressure and particle velocity with distance from the impact site. a , c , n and m are impact velocity dependent:

$$a = \alpha + \beta \text{Log}(V_{\text{imp}})$$

$$n = \lambda + \delta \text{Log}(V_{\text{imp}})$$

$$c = \gamma + \Omega \text{Log}(V_{\text{imp}})$$

$$m = \eta + \zeta \text{Log}(V_{\text{imp}})$$

A misfit value is obtained by calculating the standard deviation of a line fitted to the hydrocode data within a given region: $\epsilon = 1/N \sqrt{\sum_1^N (Y_{\text{data}} - Y_{\text{regression}})^2}$, where N is the total number of points, Y_{data} is the hydrocode result and $Y_{\text{regression}}$ denotes the value obtained by the linear regression. The zero misfit implies that the regression line is fitted to only 2 points, hence an exact fitting.

	Near Field						
V_{imp} (km/s)	a	n	misfit	c	m	misfit	
4	1.1717	-0.4530	1.074E-07	0.1276	-1.1132	3.071E-08	
5	1.3963	-0.6296	4.616E-03	0.2901	-1.0437	6.6837E-04	
6	1.5137	-0.4713	8.429E-08	0.3722	-0.8573	0.000	
7	1.6527	-0.3237	5.960E-08	0.3315	-0.4286	1.490E-08	
8	1.8093	-0.3302	5.960E-08	0.5736	-0.6567	0.000	
9	1.8853	-0.1228	8.429E-08	0.6817	-0.2156	4.214E-08	
10	1.9072	-0.1364	1.332E-07	0.7354	-0.2622	8.411E-03	

$$\alpha = 0.040, \quad \beta = 1.914, \quad \lambda = -1.214, \quad \delta = 1.058$$

$$\gamma = -0.795, \quad \Omega = 1.502, \quad \eta = -2.602, \quad \zeta = 2.368$$

630 Mid Field

631	V_{imp}	a	n	misfit	c	m	misfit
632	(km/s)						
633	4	1.3714	-0.9459	2.0576E-03	0.0917	-1.0211	3.8861E-04
634	5	1.5978	-0.9995	6.5599E-04	0.2911	-1.0402	7.3517E-04
635	6	1.6367	-0.8038	4.7266E-03	0.4143	-0.9942	8.0339E-04
636	7	1.8821	-0.9792	2.8677E-03	0.5141	-0.9563	1.8048E-03
637	8	1.9735	-0.8576	3.5979E-03	0.6750	-0.9888	6.5566E-05
638	9	2.0060	-0.7072	6.2120E-03	0.8611	-1.1259	2.0130E-03
639	10	2.0224	-0.6059	8.2497E-03	0.9317	-1.1190	1.3516E-03

640 $\alpha = 0.346, \beta = 1.736, \lambda = -1.469, \delta = 0.768$
641 $\gamma = -1.206, \Omega = 2.114, \eta = -0.864, \zeta = -0.208$

642

643

644 Far Field

645	V_{imp}	a	n	misfit	c	m	misfit
646	(km/s)						
647	4	1.5136	-1.1453	6.4139E-04	0.2397	-1.2158	1.1549E-03
648	5	1.7356	-1.1640	5.0752E-04	0.4635	-1.2389	1.0468E-03
649	6	1.9107	-1.1864	6.9751E-04	0.6248	-1.2531	1.2862E-03
650	7	2.0602	-1.2182	6.0862E-04	0.7628	-1.2783	1.3663E-03
651	8	2.2186	-1.2816	3.3932E-04	0.8936	-1.3220	1.0471E-03
652	9	2.4057	-1.3818	1.1730E-03	1.0620	-1.4091	8.7868E-04
653	10	2.5440	-1.4492	1.5957E-03	1.1887	-1.4687	1.3772E-03

654 $\alpha = -0.056, \beta = 2.558, \lambda = -0.647, \delta = -0.744$
655 $\gamma = -1.177, \Omega = 2.333, \eta = -0.818, \zeta = -0.600$

656

657

658

659

660

661

662

663

664

665

666

667

668

669

670

671

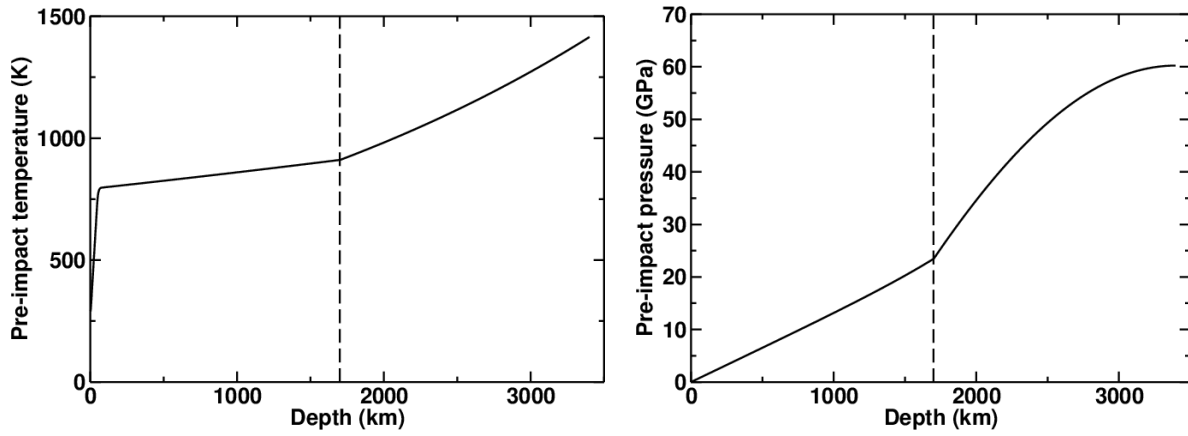
672

673

674

675

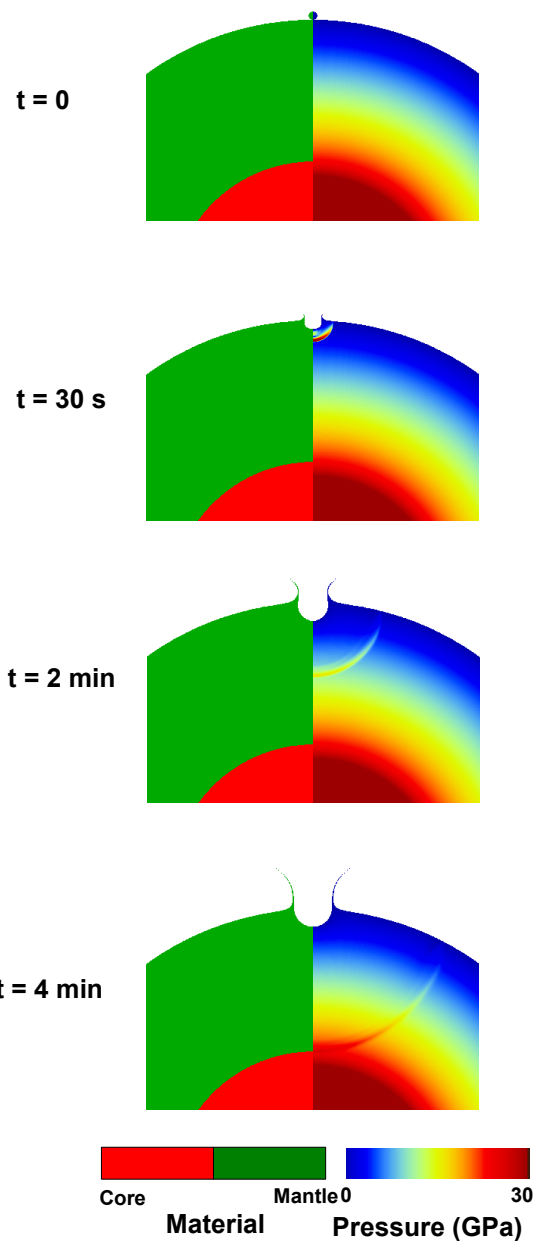
676
677
678
679
680



681
682
683
684
685
686

Figure 1

Figure 1: Pre-impact temperature (left) and lithostatic pressure (right) as a function of depth. The dashed lines illustrate the core-mantle boundary.



687
 688 **Figure 2:** A close up view of the material repartition (left column) and total pressure (right
 689 column) as functions of time (from top to bottom) in the model planet (for $V_{\text{imp}}=10 \text{ km/s}$ and
 690 $D_{\text{imp}}=100 \text{ km}$). In this model, the grid resolution is 2 km in all directions. The silicate mantle
 691 and the impactor are made of dunite.

692
 693
 694

695
696
697
698
699

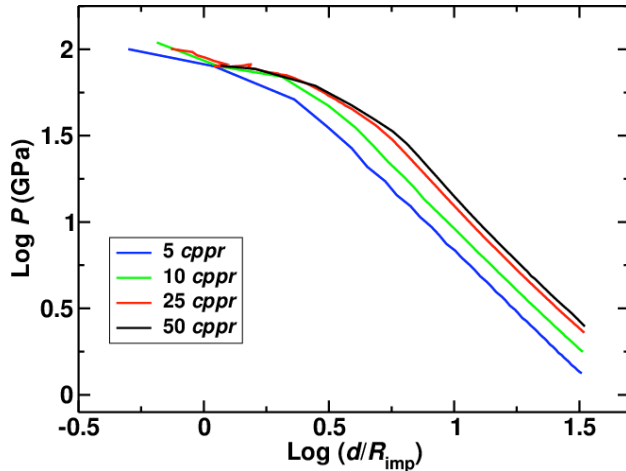


Figure 3a

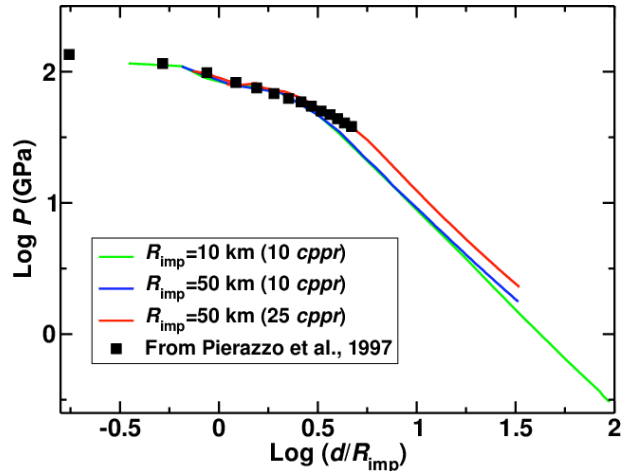
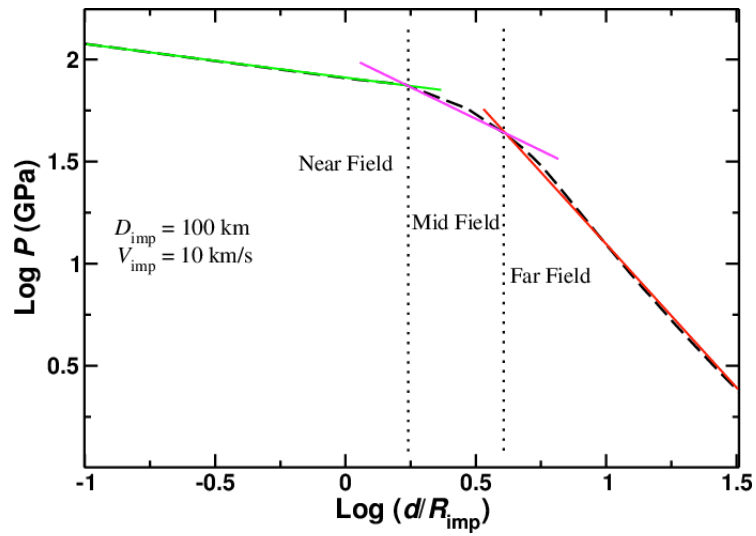


Figure 3b

700
701
702
703
704
705
706
707
708
709
710
711
712
713
714
715
716
717
718
719
720
721
722
723

Figure 3: Peak pressure decrease as a function of depth normalized by the radius of the impactor for the impact velocity of 10 km/s. The silicate mantle as well as the impactor are made of dunite. **3a:** Influence of the spatial resolution. Here we only consider the case with $R_{\text{imp}}=50$ km. The results from our hydrocode models are shown by colored curves with a spatial resolution ranging from 5 to 50 *cpr*. **3b:** Comparison of our results with $R_{\text{imp}}=50$ km (red curve, 25 *cpr*) and $R_{\text{imp}}=10$ km (green curve, 10 *cpr*) with the results from a similar model of Pierazzo et al., (1997) (black squares).

724
725
726



727
728
729
730
731
732

Figure 4. Shock pressure versus normalized distance from the impact site at the surface produced by a 100 km diameter impactor with an impact velocity of 10 km/s. The dashed curve represents the hydrocode model, while the straight lines are fitted to three different parts of the hydrocode model.

733

734

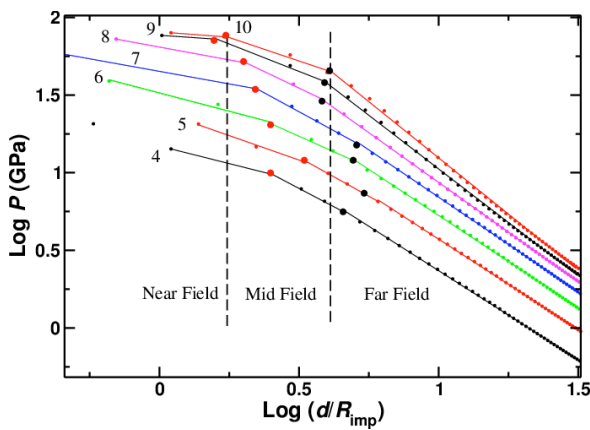


Figure 5a

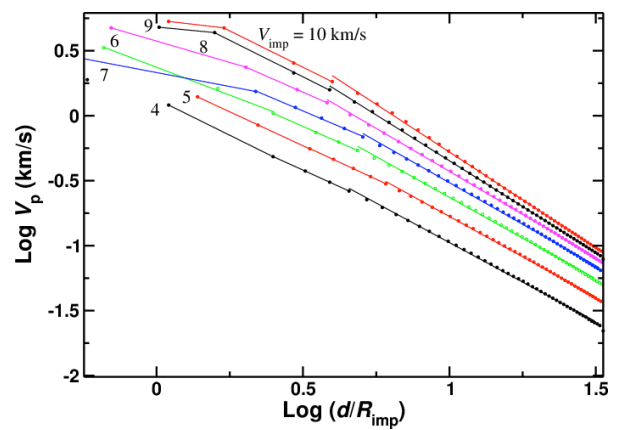


Figure 5b

735

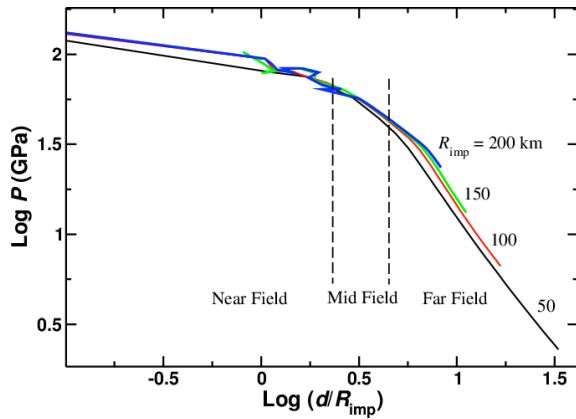
736

737

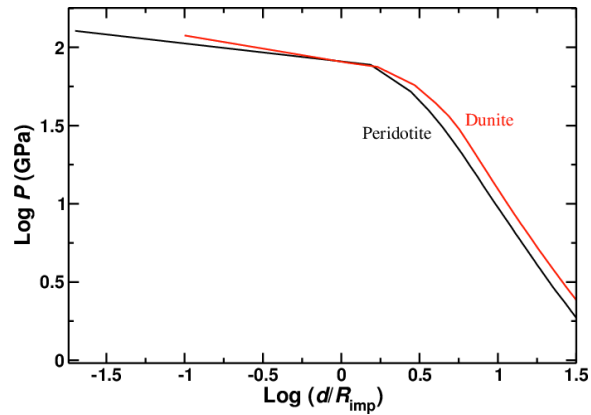
738 **Figure 5a.** Shock pressure versus normalized distance from the impact site at the surface for an
739 impactor of 100 km diameter and impact velocities ranging from 4 to 10 km/s. The numbers on
740 the curves are the impact velocities. The hydrocode results are presented by dots, while the
741 regression lines to the near field, mid field and far field regions are straight lines. The larger dots
742 show the intersections of the linear regression lines. For example a dot that separates near field
743 from mid field is the intersection of the regression lines fitted to the near field and mid field data.
744 **5b.** shows the corresponding particle velocity.

745

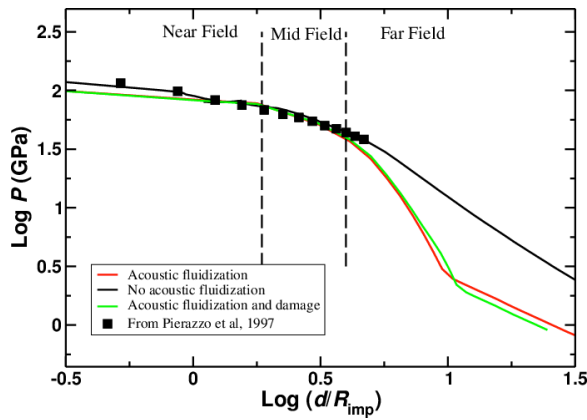
746



747
748 **Figure 6a**



749
750 **Figure 6b**



751
752 **Figure 6c**

753

754 Figure **6a.** shows the hydrocode results for impactors of 50 to 400 km diameter and impact
 755 velocity of 10 km/s. **6b.** compares the hydrocode results using dunite and peridotite as mantle
 756 rock types, for an impactor of 100 km diameter and impact velocity of 10 km/s. **6c** illustrates the
 757 shock pressure as a function of d/R_{imp} with (red curve) and without (black curve) acoustic
 758 fluidization. The green curve represents the results considering an Ivanov damage model. (For
 759 comparison, the black squares represent the results from Pierazzo et al., (1997)], which has not
 760 considered acoustic fluidization).

761

762

763
764

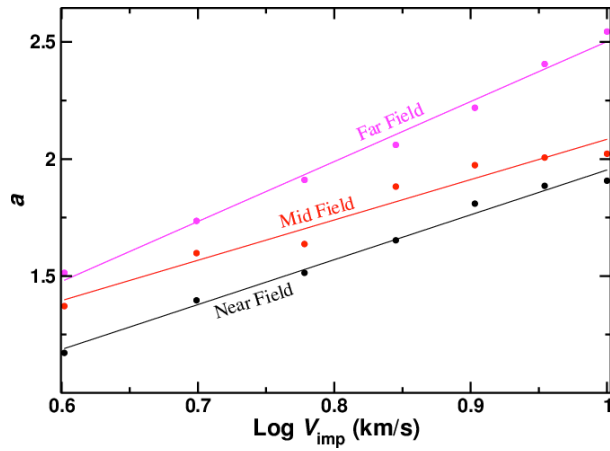


Figure 7a

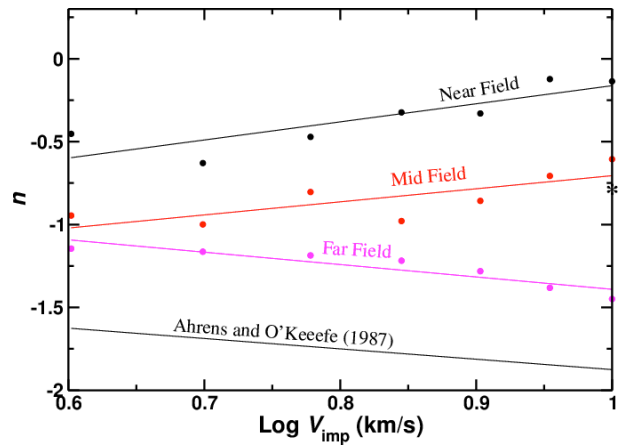


Figure 7b

765
766
767

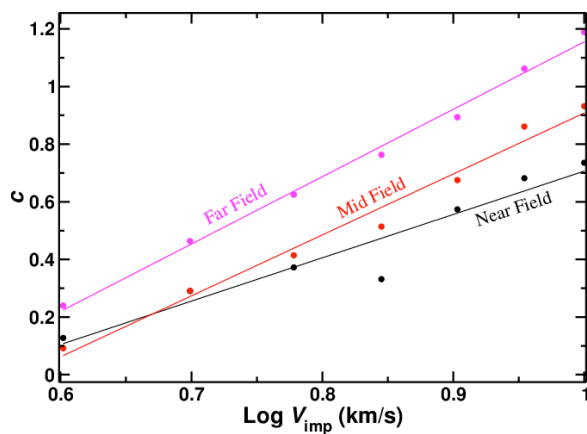


Figure 7c

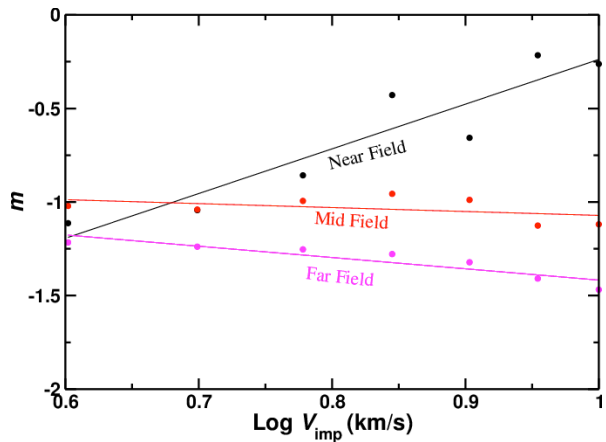
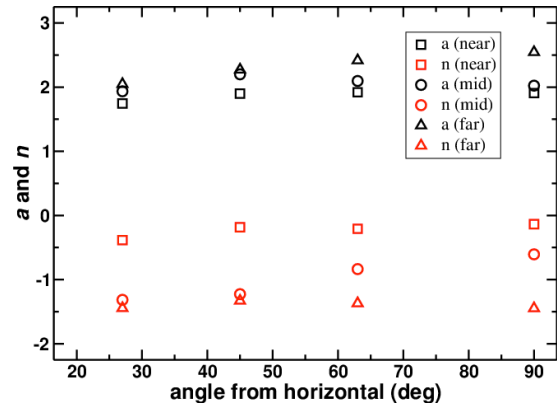
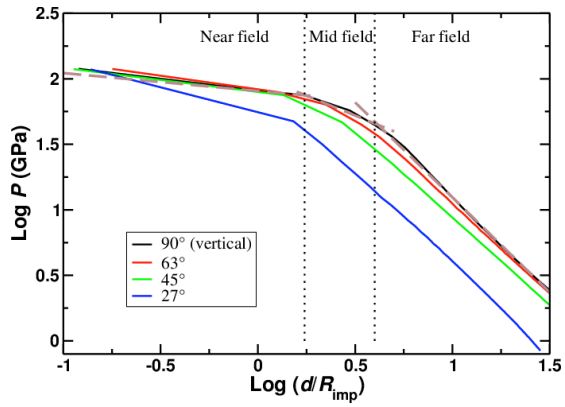


Figure 7d

768
769
770
771
772
773
774
775
776

Figure 7. Dependence of regression parameters a , n , c , and m from Eq. 4 and 5 on the impact velocity. Dots are based on hydrocode models and lines are regression fits, see Table 2



777

778

Figure 8a

Figure 8b

779

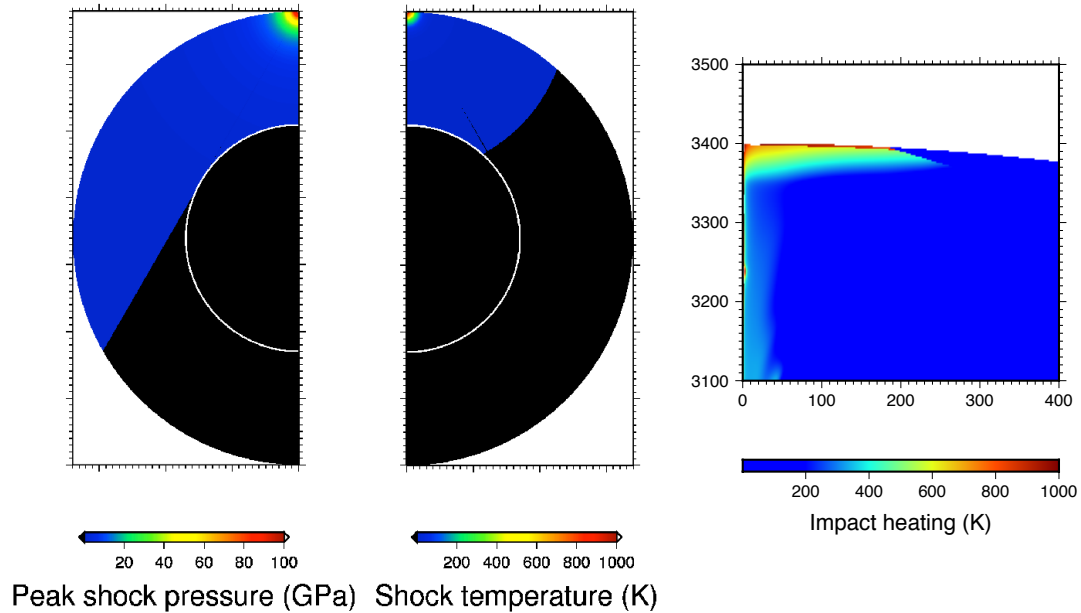
780

781

782

783

Figure 8. The shockwave propagation as a function of the angle from the horizontal for the classical case ($V_{imp}=10\text{km/s}$ and $R_{imp}=50\text{km}$). **8a** Shock pressure decrease as a function of the distance to the impact site for propagation angles ranging between 27° and 90° . **8b** Dependence of regression parameters a and n (from Eq. 4 and 5) on the angle from horizontal.

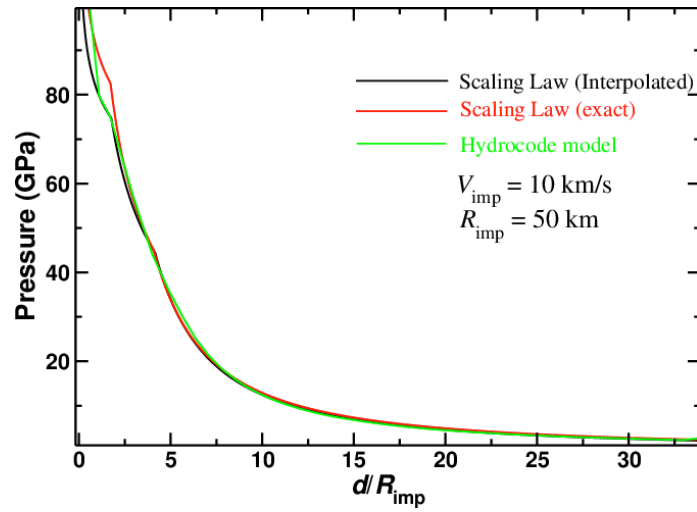


784
785

786 **Figure 9:** 2D distribution of the peak shock pressure (**left panel**), and corresponding shock
 787 induced temperature increase (**central panel**) determined from our scaling laws for an impactor
 788 of 100 km in diameter and an impact velocity of 10 km/s calculated using the scaling laws in
 789 near field, mid field, and far field and the impact-induced temperature increase model from
 790 Watters et al. [2009] (See Eq. 7-9). The parameter values are based on regression lines from
 791 Figure 7 and Table 2. The grid spacing is 2 km in radial direction and 0.03 degrees in the
 792 colatitude direction. Only direct shock wave is considered. The black region in the mantle does
 793 not receive direct waves. The thin line extending from the impact site at the surface is the
 794 tangent line to the core. It shows that the part of the core receiving direct shock wave is not more
 795 than 25%. The color is saturated at higher values to better illustrate the regions with lower
 796 values. The **right panel** shows a close-up view of the corresponding temperature increase
 797 obtained from iSALE more than 30 minutes after the impact and illustrates the modifications that
 798 occur during the late stages of the impact process (excavation, central peak formation,
 799 slumping...). However, the intensity of impact heating is in agreement with our scaling laws.

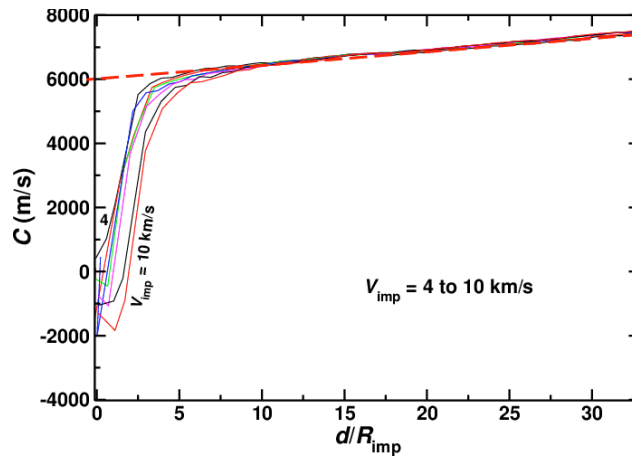
800
801
802
803

804
805
806
807



808
809
810
811
812
813
814
815
816
817
818
819

Figure 10. Shock pressure versus distance from the impact site normalized to the impactor radius. The hydrocode model is the output of the hydrocode simulation. In the exact model we have used a and n , while α , β , λ and δ are used in the interpolated model, see Table 2.



820

821 **Figure 11.** The acoustic velocity determined using Equation 10 for an impactor of 100 km
 822 diameter, and impact velocities ranging from 4 to 10 km/s. The S parameter in the equation is set
 823 to 1.2. The red dashed line is a line fit to C in the deeper region.